Full Paper

CONTRAST MEDIA & MOLECULAR IMAGING

Received: 30 December 2011, Revised: 26 July 2012, Accepted: 8 August 2012, Published online in Wiley Online Library

(wileyonlinelibrary.com) DOI: 10.1002/cmmi.1498

Evaluation of superparamagnetic iron oxide nanoparticles (Endorem®) as a photoacoustic contrast agent for intra-operative nodal staging

Diederik J. Grootendorst[a]*, Jithin Jose[a], Raluca M. Fratila[b], Martijn Visscher[b], Aldrik H. Velders[c], Bennie Ten Haken[b], Ton G. Van Leeuwen[d], Wiendelt Steenbergen[a], Srirang Manohar[a] and Theo J. M. Ruers[e,f]

Detection of tumor metastases in the lymphatic system is essential for accurate staging of malignancies. Commercially available superparagmagnetic nanoparticles (SPIOs) accumulate in normal lymph tissue after injection at a tumor site, whereas less or no accumulation takes place in metastatic nodes, thus enabling lymphatic staging using MRI. We verify for the first time the potential of SPIOs, such as Endorem® as a novel photoacoustic (PA) contrast agent in biological tissue. We injected five Wistar rats subcutaneously with variable amounts of Endorem® and scanned the resected lymph nodes using a tomographic PA setup. Findings were compared using histology, vibrating sample magnetometry (VSM) and 14 T MR-imaging. Our PA setup was able to detect the iron oxide accumulations in all the nodes containing the nanoparticles. The distribution inside the nodes corresponded with both MRI and histological findings. VSM revealed that iron quantities inside the nodes varied between 51 ± 4 and 11 ± 1 μg. Nodes without SPIO enhancement did not show up in any of the PA scans. Iron oxide nanoparticles (Endorem®) can be used as a PA contrast agent for lymph node analysis and a distinction can be made between nodes with and nodes without the agent. This opens up possibilities for intra-operative nodal staging for patients undergoing nodal resections for metastatic malignancies. Copyright © 2012 John Wiley & Sons, Ltd.

Keywords: photoacoustic imaging; lymph node staging; superparamagnetic iron oxide; optoacoustic imaging; lymph node; SPIO; photoacoustics; intraoperative

1. INTRODUCTION

Photoacoustic (PA) imaging is a hybrid imaging modality, whose ability to provide functional imaging based on physiological parameters has resulted in widespread acceptance in biomedical research applications, ranging from tumor detection to cerebral hemodynamic analysis (1). PA imaging relies on the detection of acoustic waves produced by the thermoelastic expansion of tissue following absorption of short pulsed illumination. The method combines the excellent absorption contrast achieved in optical techniques with the high spatial resolution of ultrasound imaging (2). Since biological chromophores like melanin and hemoglobin are strong optical absorbers, PA imaging provides the possibility for non-invasive imaging of these chromophores *in vivo*. The strong PA response of these chromophores enables the detection of melanoma cells (3,4) and melanoma metastases (5,6) or visualization of the vasculature associated with breast carcinoma (7) without the addition of extrinsic contrast. However, biological processes that lack an intrinsic chromophore related to a disease state, including many malignancies, would require the addition of extrinsic contrast for their detection. PA imaging, owing to its lack of ionizing radiation and fast imaging performance, could develop into an additional medical imaging method once a specific and biocompatible PA contrast agent was available.

Research into PA extrinsic contrast strategies has been going on for several years in both *in vitro* and *in vivo* models (8). Research is focused predominantly on the use of nanoparticles including gold nanorods, gold nano shells and carbon nanotubes (9–13). Yang *et al.* showed that gold nanocages can be used to map sentinel lymph nodes (14) and enhance the optical absorption

* *Correspondence to: D. J. Grootendorst, Biomedical Photonic Imaging Group, MIRA Institute, University of Twente, PO Box 217, 7500 AE Enschede, The Netherlands. E-mail: d.j.grootendorst@utwente.nl*

a *D. J. Grootendorst, J. Jose, W. Steenbergen, S. Manohar*
Biomedical Photonic Imaging Group, MIRA Institute, University of Twente, PO Box 217, 7500 AE Enschede, The Netherlands

b *R. M. Fratila, M. Visscher, B. Ten Haken*
NeuroIMaging group, MIRA Institute, University of Twente, PO Box 217, 7500 AE Enschede, The Netherlands

c *A. H. Velders*
Biomedical Chemistry, MIRA Institute, University of Twente, PO Box 217, 7500 AE Enschede, The Netherlands

d *T. G. Van Leeuwen*
Biomedical Engineering and Physics, Academic Medical Center, University of Amsterdam, PO Box 2270, 1100 DE Amsterdam, The Netherlands

e *T. J. M. Ruers*
Nanobiophysics Group, MIRA Institute, University of Twente, PO Box 217, 7500 AE Enschede, The Netherlands

f *T. J. M. Ruers*
Netherlands Cancer Institute, Antoni van Leeuwenhoek Hospital (NKI-AVL), PO Box 90203, 1006 BE Amsterdam, The Netherlands

in the cerebral cortex of mice (15), while De La Zerda demonstrated that tumors in mice can be enhanced and imaged *in vivo* using antigen coupled single-walled carbon nanotubes (16). These newly developed particles show great potential to enhance contrast with regard to several pathological problems, including cancer.

However almost all of these contrast agents are still in the experimental stage, and few clinical studies have been initialized in recent years. At this point, it is as yet uncertain if these particles will obtain clearance by the Food and Drugs Administration (FDA) and the European Medicines Agency (EMA) in the near future. Recent studies with gold nano shells (17,18) have led to the initiation of a clinical trial using gold nano shells as photo-induced hyperthermia agents for cancer therapy in patients with oropharyngeal malignancies; however it may take several years to acquire all of the results. A PA contrast agent that has already been clinically established would require a less extensive follow-up, facilitating a fast implementation in the clinic.

With respect to extrinsic contrast enhancement, magnetic resonance imaging (MRI) is one of the areas that have seen major developments in the recent years. In 1989, Weissleder *et al*. (19) used dextran-coated superparamagnetic iron oxide (SPIO) nanoparticles for nodal contrast enhancement in MRI. After subcutaneous administration of 20 μmol/kg SPIO in the footpad of healthy and tumor-bearing rats, it was shown that non-metastatic nodes appeared dark in MR images while the metastatic nodes appeared iso- or hyperintense. This image contrast difference is based on the selective uptake of the nanosized particles in non-metastatic nodes by the process of phagocytosis by macrophages (20). After subcutaneous injection, SPIOs are cleared by draining lymphatic vessels and transported to the regional lymph nodes where they are phagocytosed by nodal macrophages in a scavenger receptor-mediated endocytosis pathway (21,22). In MRI, locations containing SPIOs then show up as areas of reduced signal intensity because of the magnetic susceptibility of the particles. If metastases cause disturbances in nodal flow or displace nodal macrophages, the uptake of SPIOs inside the node is decreased and the node will contain less iron oxide, appearing iso- or hyperintense. Most importantly, the inhomogeneities in the MRI contrast patterns within the node are shown to correlate with the locations of metastatic deposits, enabling staging on the outlook of the SPIO distribution within a node.

The oncologist's decision to use neoadjuvant therapy or the surgeon's decision to perform nodal dissection is influenced by the presence or absence of lymphatic metastases and therefore the use of SPIOs to improve pre-operative nodal staging has been extensively researched. Coated iron oxide nanoparticles have been found to contain a satisfactory safety profile for human applications (23) and, as a result, several iron oxide dispersions have been cleared for clinical use. Preoperative nodal staging for different malignancies is known to benefit from the use of these dispersions (24–27).

Our work regarding the detection of melanoma metastases in resected human lymph nodes proved that metastases could be visualized using PA imaging (5,6). However, while melanoma metastases contain melanin, a strong optical absorber, other malignancies spread across the lymphatic system without such an intrinsic chromophore. The fact that SPIOs could function as nodal staging agents, possess large optical cross-sections (28) and proved to be photoacoustically detectable in phantoms (29), prompted us to study these particles. We investigated the PA contrast potential of iron oxide nanoparticles using an animal model to explore the possibilities of detecting the accumulated nodal deposits of these particles after subcutaneous injection. The detection of these deposits could allow for resected lymph nodes to be photoacoustically scanned for metastatic involvement in the operation theatre, saving time and possibly preventing the recall of a patient for an additional operation. A concept also explored by other optical techniques like optical coherence tomography (30) and Raman spectroscopy (31).

2. MATERIALS AND METHODS

2.1. Iron Oxide Nanoparticles

We used the commercially available SPIO agent Endorem® (Guerbet, Villepinte, France) (Fig. 2A), comprising iron oxide nanoparticles (11.2 mg/ml) dispersed in water. The particles are composed of several iron oxide cores (diameter 4–6 nm) embedded inside a dextran coating (32). Particles have an estimated hydrodynamic size of 80–150 nm (33). Dilutions were prepared using sterile phosphate buffered saline (PBS).

2.2. Animals

A rodent model was implemented to mimic the human lymphatic situation. The animal research protocol was approved by the animal ethics committee of the University Medical Center Utrecht.

Five mature female Wistar rats, weighing approximately 250–300 g were housed at the animal facility of the University of Twente and fed according to normal procedures, including grouped housing, nesting material and free access to food and water. Swelling of the lymph nodes, required to obtain a nodal volume that could be easily resected and imaged, was achieved by a subcutaneous injection of 0.1 ml of incomplete Freund adjuvant (IFA) (34) inside both footpads of the hind legs. IFA is composed of a water in oil emulsion and functions as immunopotentiator to achieve macrophage activation and immune cell multiplication, leading to an increase in lymph node size. In addition, in a future clinical situation nodes are likely to show tumor induced reactive lymphadenopathy which, according to Klerkx *et al*. (35), can be mimicked using IFA. The use of IFA will therefore result in an immune response that more closely resembles the lymphatic system in cancer patients. After 7 days, a significant increase in size was achieved and the animals were subcutaneously injected with 0.1 ml of the SPIO contrast agent in one or both footpads of the hind legs. The animals were euthanized by cervical dislocation 24 h after injection and the popliteal lymph nodes of both legs were excised. Once excised, all lymph nodes were photographed and placed inside a PBS solution. PBS prevented swelling of the tissue owing to water inflow and ensured proper PA imaging of the nodal volume over time.

Weissleder *et al*. (19) subcutaneously injected approximately 3.2 mg iron oxide in their initial study in rats to verify the potential of the nanoparticle agent. In order to find out if PA detection of the nodes could be done with smaller SPIO concentrations, we also administered several dilutions of the Endorem® stock solution. The five animals were subcutaneously injected in the following way:

1. In one animal no contrast agent was injected (control).
2. In two animals undiluted (1.12 mg iron oxide) Endorem® was injected in the left footpad.

3. In one animal both footpads were injected with a ×2 dilution (0.56 mg iron oxide).
4. In one animal both footpads were injected with a ×4 dilution (0.28 mg iron oxide).

A total of 10 lymph nodes were included in the study of which six were suspected of containing iron oxide nanoparticles (contrast nodes) and four were not (control nodes).

2.3. PA imaging

Resected nodes were placed inside a hollow transparent 3% Agar sample holder with an inner diameter of 25 mm and wall thickness of 10 mm. The sample holder was placed in the center of a large water container where it was illuminated from the top. The detector was placed orthogonal to the light illumination and rotated around the object to acquire a tomographic measurement. While details of the instrument have been presented earlier (36), we describe here the essentials. The PA setup (Fig. 1) consists of a Q-switched Nd:YAG laser (Brilliant B, Quantel, France) with an optical parametric oscillator (Opotek, 700–950 nm) operating at a 10 Hz repetition rate. Irradiation intensity can be varied up to 40 mJ/cm^2. The light is delivered via a beam expander creating a beam diameter of around 1 cm to cover the entire specimen under investigation. The photoacoustic signals are recorded with a curvilinear detector array (Imasonic, Besançon) consisting of 32 elements and shaped to 85° of a circle of 40 mm radius. The center frequency of the array is 6.25 MHz with a reception bandwidth >80%. Individual elements have sizes of 10 by 0.25 mm. These elements are arranged with an inter-element spacing of 1.85 mm. At each position signals are acquired from the detector using a 32 channel pulse-receiver system (Lecoeur Electronique, Paris) with a sampling rate of 80 MHz. Filtered acoustic backprojection was used to reconstruct the PA images off-line (36).

Before the start of scanning procedure, the setup was calibrated using an agar phantom containing four horse tail hairs to ascertain the tomographic geometry. All nodes were fixed with a small amount of ultrasound gel to prevent floating and disruptive movements. Once fixed, the position of the node was checked by visual examination and air bubbles around the sample were removed. The temperature of the water in the PA tank was monitored throughout the experiment to avoid image reconstruction irregularities caused by a change in the speed of sound.

All scans were performed using an irradiation intensity of around 15 mJ/cm^2, a wavelength of 720 nm and 20 projections. While 720 nm is not an exclusive wavelength (Fig. 2B), we can identify at this wavelength a low absorptionof total hemoglobin coupled with a significant absorption of the dispersion. Further, absorption by fat (and water) is negligible (2). In addition, our previous research (5) shows that the large penetration depth of near-infra-red illumination also contains an advantage for the imaging of larger nodes and nodes that contain significant amounts of extranodal fat.

2.4. Magnetic Resonance Imaging

Verification of the PA contrast results with regard to the presence of iron oxide nanoparticles and their distribution in the node was performed using a 14 T MRI system (Bruker, Ettlingen,

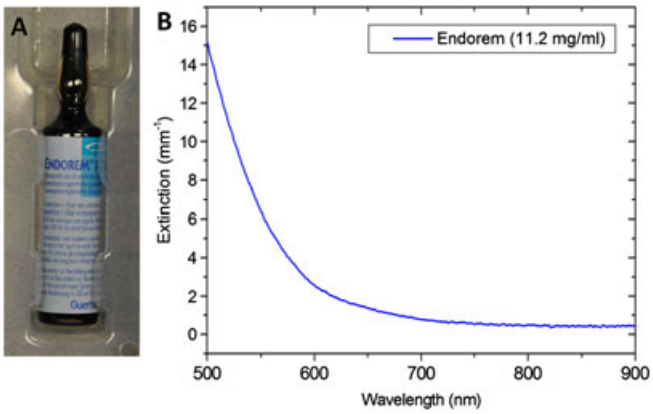

Figure 2. A: Photograph of an Endorem® vial displaying the dark color of the dispersion B: The extinction spectrum of an Endorem® dispersion.

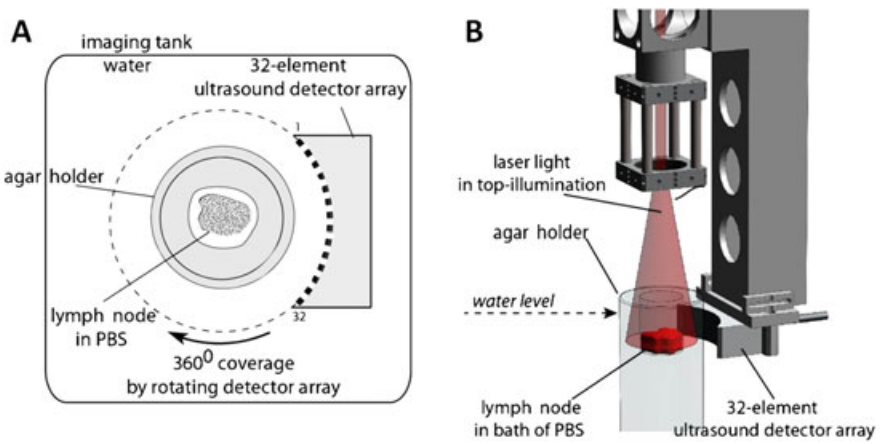

Figure 1. A: A top view of the tomographic photoacoustic setup utilizing top illumination. B: A three dimensional schematic of the setup. The holder containing the lymph node is illuminated from the top while the ultrasound detector is rotated around the holder. The water in the imaging tank ensures ultrasound transmission to the detector. (*Reprinted with permission of the Journal of Biomedical Optics. Initial results of imaging melanoma metastasis in resected human lymph nodes using photoacoustic computed tomography, J.Jose, D.J. Grootendorst, T.W. Vijn, M.W. Wouters, H. Van Boven, T.G. Van Leeuwen, W. Steenbergen, T.J.M. Ruers, S. Manohar. 16(9), 096021, 2011*).

Germany). The system was equipped with a vertical narrow bore magnet (14.1 T), a B_0 compensation unit (BGU-II) and three 1/60 amplifier units (*X*, *Y* and *Z*). A micro-imaging probe, equipped with a 10 mm diameter saddle coil insert, was used. All experiments (acquisition and processing) were carried out using ParaVision (version 4.0)/Top Spin (version 1.5) software. The nodes were fixated in 4% buffered formaldehyde after PA imaging and transferred to quartz NMR tubes with a diameter of 10 mm. All nodes were positioned in such way to ensure that the orientation corresponded to that of the PA scans.

The iron oxide nanoparticles shorten both T_2 and T_1 relaxation times, which results in a signal loss at locations of the SPIOs inside the lymphatic tissue. A multi-slice–multi-echo (MSME) imaging sequence was used with an echo time of 10 ms and a repetition time of 1000 ms. The sequence produces a larger longitudinal and transverse magnetization, making the surrounding fat appear bright, facilitating nodal identification and SPIO distribution analysis in the imaged volume. Images were acquired using a matrix dimension of 256×256, a field of view of 1 cm and a slice thickness of 0.5 mm. Signal averaging was varied between 5 and 10, based on the quality of the acquired image.

2.5. Vibrating Sample Magnetometry

The amount of iron oxide inside the lymphatic tissue was quantified with a vibrating sample magnetometer (Quantum Design, San Diego, CA, USA) with a variable magnetic field of ± 4 T. Nodes were kept inside the quartz NMR tubes and strongly fixated to ensure no movement occurred owing to the vibrations of the device. Measurements were checked for movement artifacts and all results were correlated to three reference samples containing a known amount of iron oxide. A standard deviation and average iron oxide amount were then calculated.

2.6. Optical Property Estimation

Based on the iron quantities measured within the nodes using vibrating sample magnetometry (VSM), we aimed to estimate the optical absorption coefficient μ_a (1/mm). To this end, interaction efficiencies (extinction, scattering and absorption) were estimated using Mie theory (37) for a core radius of 2.5 nm and a shell radius of 15 nm (32), with dielectric data for iron oxide and dextran from Schlegel *et al*. (28) and Butler (38). Results indicated that the scattering component of the extinction was small compared with the absorption component. Spectroscopy (UV-2401PC spectrophotometer, Shimadzu, Tokyo, Japan) on a diluted Endorem dispersion (0.56×10^{-6} g/mm^3) was used to measure the extinction coefficient μ_{ext} (1/mm) at 720 nm and, by correlating the μ_{ext} to the iron quantities within each node divided by the nodal volume, an estimation of the μ_a within each node was produced. The volume within each node was calculated using the MRI slice dimensions.

In addition, the PA contrast of SPIO particles was compared with that of whole human blood by embedding the measured iron amounts inside a phantom. By taking the lowest and highest iron amounts measured within the nodes and dividing them by the nodal volume, an estimation of the SPIO concentration within the nodal tissue could be made. The estimated concentrations were diluted from the stock dispersion and injected into two nylon tubes (i.d. 1 mm, o.d. 1.8 mm). These were embedded one-by-one, into a 2% agar phantom in which a similar tube containing unclotted whole human blood was placed, as depicted in Fig. 5(A). By measuring the average PA response of the tubes, the contrast between both could be quantified.

2.7. Histology

To verify the presence of SPIOs inside the lymphatic tissue, additional histological analysis of several nodes was performed using a Pearls Prussian Blue stain (Sigma-Aldrich, St Louis, MO, USA). The nodes were embedded in paraffin and cut into 5 μm slices. Special attention was paid to the orientation of the cutting surface, which was kept parallel to the imaging plane of both the PA as the MR image. After staining, the slices were imaged and photographed using a bright field optical microscope (Nikon E600, Tokyo, Japan).

3. RESULTS

During the experiments none of the animals experienced visual signs of discomfort following both IFA and Endorem® injections. Some licking of the hind legs was noted directly after injection; however, all animals functioned normally during the subsequent days. Injection of the different Endorem® solutions into the hind leg of the animals entailed a visible discoloring throughout the lower part of the injected leg. After excision a dark discoloring of all of the popliteal lymph nodes draining the hind leg in which Endorem® was injected was observed, while lymph nodes from hind legs without Endorem® administration did not possess this discoloring. All nodes had diameters of around 3–5 mm and most contained some extranodal fat.

Figure 3 shows the PA images of a contrast and a control node (A–C) together with corresponding photographs of the nodes in their imaged positions (D–F). Figure 4 shows PA and MR images of all contrast nodes and demonstrates their correlation in contrast distribution. PA imaging of the individual nodes showed bands of clear signal increase in the periphery of the nodes suspected of containing SPIOs (Figs 3A and 4, columns 1 and 3). Almost no signal enhancement was noted in the center of these nodes, although some contained larger signal poor areas then others. No significant increase in signal was noted in the popliteal nodes excised from hind legs not injected with Endorem® (control nodes), corresponding with the absence of discoloring noted after excision (Fig. 3B). The image of both the control and the contrast containing node shows this clear distinction in PA response (Fig. 3C). The small centers of absorption in the PA image of the control node (Fig. 3B) are possibly small blood droplets in the extranodal fat caused by the surgical resection. Although small amounts of Endorem®, up to 0.28 mg, were injected (Fig. 4(5,6), Table 1), all nodes suspected of containing SPIOs showed enough PA signal to be distinguished from nodes without contrast injection.

MR images (Fig. 4, columns 2 and 4) showed a clear signal decrease in all discolored nodes, largely located in the periphery of the nodal volume. Distribution of this decrease corresponded with the areas showing PA response in most cases. Almost all nodes showed only a small decrease in signal in the center of their anatomy. Calculation of the dimensions of all nodes using the MR information revealed a strong correlation with the dimension calculations based on the PA scans (Table 2). MRI of the control nodes showed no significant decrease in signal throughout the nodal volume corresponding to a lack of SPIOs.

Vibrating sample magnetometry measurements showed the presence of a superparamagnetic contrast agent inside all nodes suspected of contrast inclusion, although the amounts varied between the nodes. Table 1 displays the amount of iron oxide measured by VSM inside each node together with the estimated absorption coefficients. The highest iron quantity was measured in node 2 at $51 \pm 4\,\mu g$, while the lowest quantity was determined in node 6 at $11 \pm 1\,\mu g$. The control nodes obtained from the

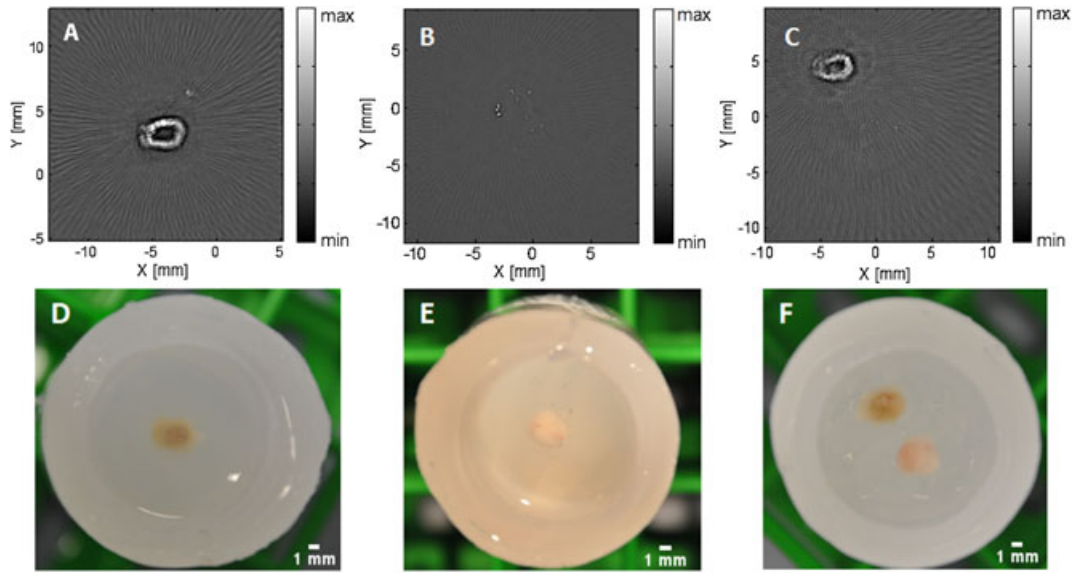

Figure 3. A: Photoacoustic image of lymph node containing Endorem®. B: PA image of control node. C: PA image of both the control and the Endorem® containing node. D: Photograph of lymph node containing Endorem®. E: Photograph of control node. F: Photograph of both the control and the Endorem® containing node.

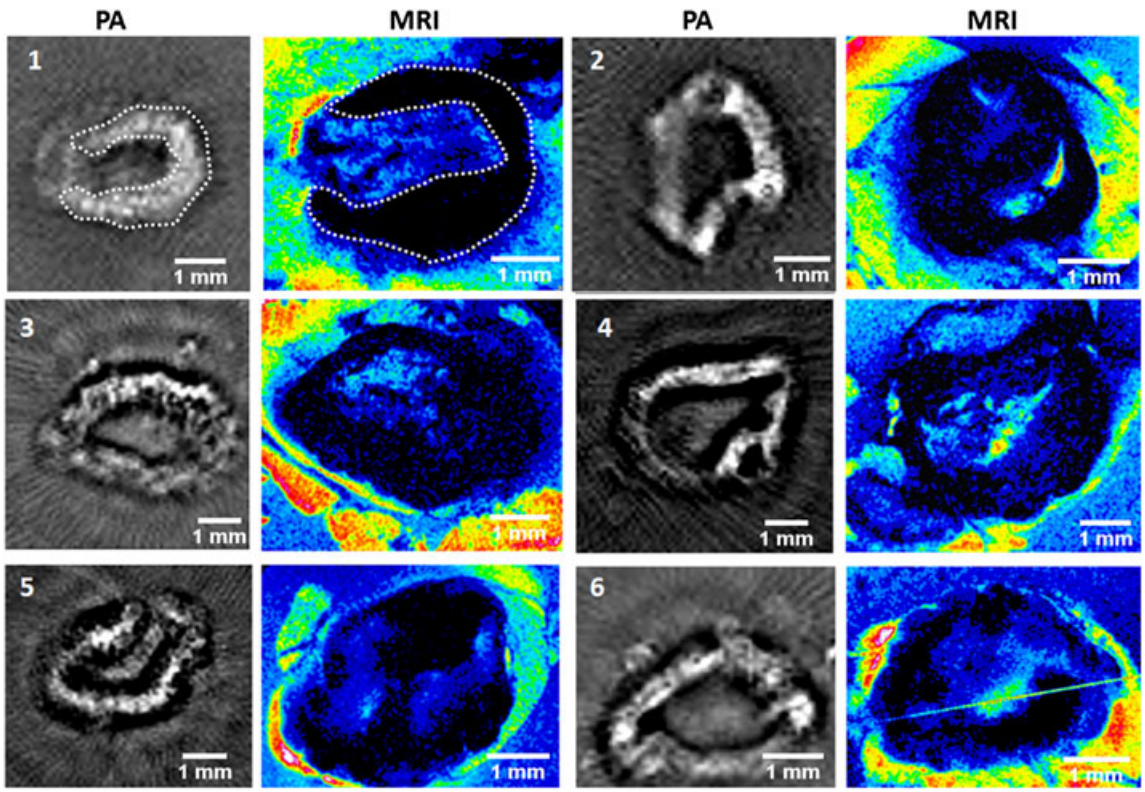

Figure 4. Photoacoustic and MR image comparison of all resected lymph nodes with contrast injection. As shown in lymph node 1 (white dotted line), the PA response pattern is comparable with the location of MRI signal decrease. Some nodes show a continuous contrast band throughout their periphery (1,5), while others show some small irregularities (4,6).

animals subjected to contrast injections at the contralateral limb showed the presence of very small deposits of iron, up to 1 μg, while the nodes from the control animal did not display any superparamagnetic behavior. Based on these amounts, the estimated μ_a of the contrast nodes varied between 0.27 and 0.06/mm. By taking the nodal dimensions measured by MRI into account, the highest (51 μg) and lowest (11 μg) iron amounts correlated to SPIO concentrations of 3.6 and 0.8 mg/ml. PA measurement of these concentrations and whole human blood showed an average PA response of 23 for blood compared with a response of 15 and 49 for respectively the low and high concentration samples (Fig. 5B).

Histology (Fig. 6) confirmed the presence of significant iron deposits throughout the nodes suspected of nanoparticle inclusion. Iron presence was most pronounced inside macrophages located in the periphery of the nodes. No significant presence of iron was revealed by the histological assessment of the control nodes (Fig. 6D).

Table 1. Lymph nodes sorted by number with their corresponding iron quantities and estimated absorption coefficients at 720 nm

Number	Injected iron (μg)	Iron inside the node (μg)	μ_a (1/mm)
1	1120	27 ± 2	0.14 ± 0.01
2	1120	51 ± 4	0.27 ± 0.02
3	560	40 ± 3	0.21 ± 0.02
4	560	49 ± 3	0.26 ± 0.02
5	280	30 ± 2	0.15 ± 0.01
6	280	11 ± 1	0.06 ± 0.01
7–10	0	0 ± 1	±0

Table 2. Calculated maximal and perpendicular diameters of all lymph nodes based on both photoacoustic (PA) imaging and MRI. Lymph nodes sorted by number. Measured sizes contain error margins of ± 0.3 mm. PA dimensions of nodes 7–10 could not be calculated because of their lack of PA response

	PA based diameter		MRI based diameter	
Number	Maximal (mm)	Perpendicular (mm)	Maximal (mm)	Perpendicular (mm)
1	3.5	3.0	3.5	3.0
2	4.1	2.8	3.4	2.8
3	4.5	2.8	4.5	2.8
4	4.1	2.6	4.1	2.9
5	4.0	3.3	4.2	2.9
6	3.5	2.6	3.4	2.6
7	—	—	3.5	2.6
8	—	—	3.3	2.8
9	—	—	3.9	3.1
10	—	—	3.4	3.2

4. DISCUSSION AND CONCLUSIONS

The results obtained from the animal model show that PA imaging can be used to detect the presence of iron oxide nanoparticles inside lymphatic tissue. Subcutaneous injection of Endorem® did not produce any negative side effects in the animals, giving an indication that the safety profile may potentially be favorable for subcutaneous applications in humans. The effects of the IFA injection to initiate nodal swelling enabled us to easily pinpoint and extract the popliteal node while ensuring that both imaging techniques would be able to map the contrast agents accumulation. Weissleder *et al.* (19) showed that the distribution and amount of iron in these so-called hyperplastic nodes are similar to those of normal nodes, which indicates that the uptake of these nodes is not significantly altered by the adjuvant.

Predominant PA signal generation was noted in the periphery of the nodes, which coincides with the location of the peripheral sinusoidal macrophages. MRI shows clear loss of signal in corresponding regions in the nodes, confirming that most of the iron oxide nanoparticles are located at these locations. The histologic presence of iron particles in the periphery of the nodes confirms the imaging results and demonstrates that the contrast agent is distributed selectively at the margins of the lymphatic tissue. An explanation for this phenomenon is given by Lee *et al.* (39), who also noted signal loss in the periphery of their unenlarged

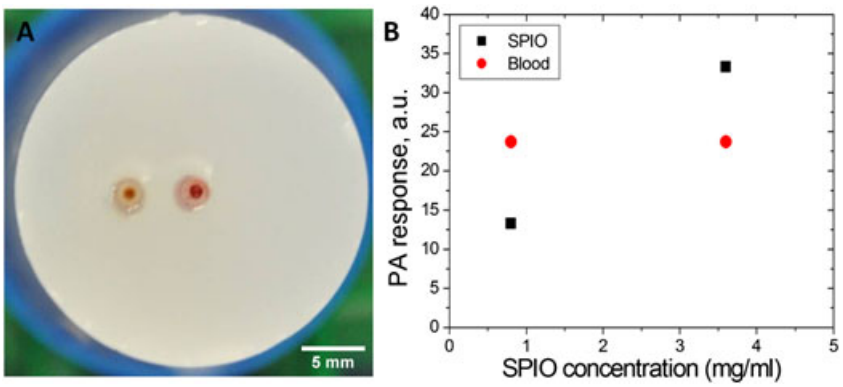

Figure 5. Phantom measurement of the amount of PA contrast generated within the node compared to that of whole blood. A: Photograph of the agar phantom containing one tube filled with different concentrations of SPIO particles (left) and one tube filled with whole human blood (right). B: The average PA contrast measured within the tubes for a SPIO concentration of 0.8 and 3.6 mg/ml. At a SPIO concentration of 3.6 mg/ml the PA response is higher than that of blood.

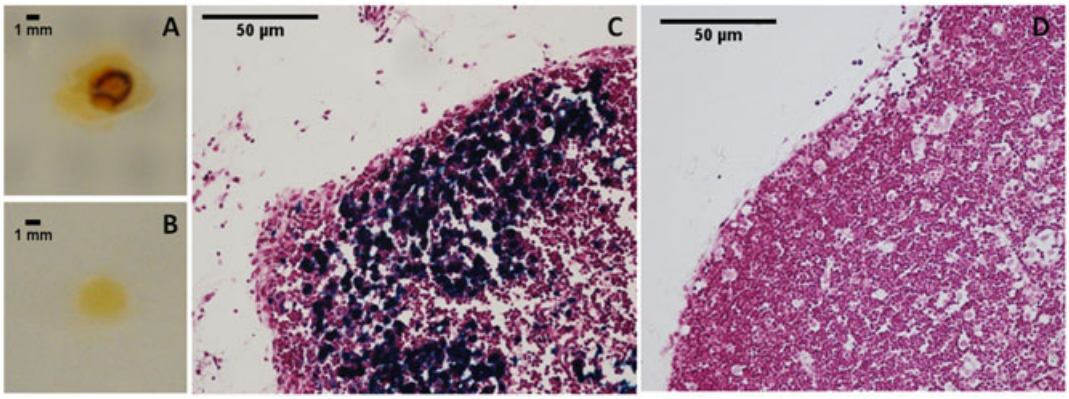

Figure 6. A: Photograph of a paraffin section of a contrast node showing a dark discoloring in its peripheral zone (node 1). B: Photograph of a paraffin section of a control node showing no significant discoloring (node 7). C: Prussian Blue stained microscopic image of a contrast node (node 1) (Magnification 20×) showing iron deposits in the periphery of the node D: Prussian Blue stained microscopic image of a control node (node 7) (Magnification 20×) showing no iron deposits.

rat nodes using 9.4 T MR imaging and Prussian blue staining. Their analysis suggested that the predominant accumulation of iron oxide nanoparticles in the peripheral sinusoidal macrophages lining the subcapsular sinuses gave rise to this phenomenon. The larger size of the Endorem SPIO particles in comparison to the particles used in their study could have further facilitated the retention of the particles in the nodal periphery. However, an inhomogeneous distribution was also noted by Lind *et al.* (40) using SPIOs with a larger hydrodynamic size.

Prussian blue stained histology indicated that some nodes did contain smaller iron deposits in their medullary sinuses or less pronounced iron presence in their periphery compared with the imaging results. It should be noted, however, that histology is less sensitive to the presence of iron oxide nanoparticles than MRI, making a point-to-point comparison between histological slices and images difficult to produce in most situations.

Iron quantity analysis using vibrating sample magnetometry revealed that the amount of iron present in each node varied significantly between animals. No clear relation could be established between the amount of iron injected and the amount of iron captured within the nodal volume. In addition, the average PA response within the contrast band in each node could not be correlated to the corresponding measured iron amount. This is most likely due to the differences in extranodal fat covering each sample, which leads to the fluence at the slice carrying the signal band being different. However, our results show that the location of the contrast agent could still be verified at a quantity as low as $11 \pm 1\,\mu g$, indicating that, if the human situation showed less nodal uptake, it could still be possible to perform accurate nodal staging. The phantom measurements indicate that the amount of PA response of SPIO deposits mainly depends on the quantity in which it is present in the nodes and that at higher concentrations they produce more PA signal than human blood. However, as shown by our VSM measurements, the amount of iron obtained within the nodes is variable, so it remains unclear whether an *in vivo* approach could clearly visualize the characteristics of the absorption patterns mentioned (29). The influence of other biological structures is limited in an *ex vivo* intra-operative staging setting, which therefore should be the first clinical application goal of the technique. The estimated absorption coefficients show that the optical absorption of the tissue is increased owing to the inclusion of the nanoparticles. The estimated amounts of absorption do not impede the penetration of optical energy into lower parts of the node, indicating that metastases that are located deeper within the node could also be visualized.

Since normal lymphatic tissue displays low absorption at 720 nm, the nodal outline and size could not be distinguished in nodes 7–10 (Table 2); however, the dimensions and shape extracted from the PA images of the nodes containing SPIOs match those estimated from MRI. An accurate depiction of nodal size using SPIO-enhanced PA imaging could function as an additional indicator of possible metastatic involvement, because larger nodes (≥1 cm) are more likely to include metastases (41). The fact that nodes without SPIOs do not produce recognizable PA response patterns could imply that nodes that are totally filled with malignant cells will also not show up on PA measurements. In these cases, clinical staging has to be performed on images without distinguishable features, which could create some problems with regard to specificity. However, in the case of a sentinel node biopsy, an additional colored tracer, spreading homogeneously through the node, is always injected for locating the actual sentinel node. Multiple wavelength imaging (42,43) could in this case provide us with a nodal outline based on the colored tracer while staging decisions could be made on the images of a wavelength sensitive for the SPIO contrast agent. In nodes with smaller metastases, macrophages will be replaced by tumor cells in specific parts of the node. These tumor deposits occupying regions as small as 2 mm in the node have been proven to be detectable in MR studies (44–46). Likewise in PA images, smaller metastases could be detectable based on spatial features showing low intensities. How sensitively these features can be visualized in PA needs to be investigated in future experiments using a metastatic model.

The detection of SPIOs in lymphatic tissue using PA imaging offers possibilities for distinguishing nodes with nanoparticle deposits from nodes lacking uptake. Future research should verify if the difference in uptake between malignant and benign nodes can be visualized using PA imaging, creating opportunities for fast intra-operative nodal staging. Detection of iron oxide nanoparticles using PA imaging can prove especially promising once other types of iron oxide-based agents enter the clinic. A combination of diagnostic pre-operative imaging using MRI and intra-operative staging using PA imaging could be performed and the translation of PA imaging into the clinic would also benefit from a direct comparison of the results with

an established imaging method like MRI. Moreover, the magnetic properties of the SPIOs could also be used to influence photoacoustic signals, thereby generating additional biological information and considerably improving specificity (47–49). Although our *ex vivo* study mainly shows the potential for intra-operative imaging, non-invasive high-resolution PA lymph node mapping (50,51) after SPIO injection for superficial nodes could also be investigated, although it remains unclear if SPIO particles provide sufficient *in vivo* contrast for such an application.

We conclude that iron oxide nanoparticles are able to enhance PA response in lymph nodes because of their active uptake by nodal macrophages in locations unaffected by metastatic cells and therefore have the potential to be implemented as a PA contrast agent for nodal staging purposes. Further research using a metastatic model should show if PA imaging based on these nanoparticles is able to produce reliable indicators for the presence of metastatic deposits.

Acknowledgements

We acknowledge the contribution of Professor R. J. A. van Wezel (UMC Utrecht) for his insights during the application of our animal protocol and thank Ms B. Klomphaar for her help regarding animal care. The work was funded through through the PRESMITT project (IPD067771) of the AgentschapNL program IOP Photonic Devices.

REFERENCES

1. Li C, Wang LV. Photoacoustic tomography and sensing in biomedicine. Phys Med Biol 2009; 540(19): R59–R97.
2. Beard P. Biomedical photoacoustic imaging. Interface Focus 2011; 1(4): 602–631.
3. Zharov VP, Galanzha EI , Shashkov EV, Khlebtsov NG, Tuchin VV. *In vivo* photoacoustic flow cytometry for monitoring of circulating single cancer cells and contrast agents. Opt Lett 2006; 31(24): 3623–3625.
4. Weight RM, Dale PS, Viator JA. Detection of circulating melanoma cells in human blood using photoacoustic flowmetry. In Engineering in Medicine and Biology Society. Annual International Conference of the IEEE: New York, 2009; 106–109.
5. Jose J, Grootendorst DJ, Vijn TW, Wouters M, van Boven H, van Leeuwen TG, Steenbergen W, Ruers TJM, Manohar S. Initial results of imaging melanoma metastasis in resected human lymph nodes using photoacoustic computed tomography. J Biomed Opt 2011; 16: 096021.
6. Grootendorst D, Jose J, Van der Jagt P, Van der Weg W, Nagel K, Wouters M, Van Boven H, Van Leeuwen TG, Steenbergen W, Ruers T. Initial experiences in the photoacoustic detection of melanoma metastases in resected lymph nodes. Proc SPIE 2011; 7899: 78993J.
7. Piras D, Xia W, Steenbergen W, van Leeuwen TG, Manohar SG. Photoacoustic imaging of the breast using the Twente photoacoustic mammoscope: Present status and future perspectives. IEEE J Sel Top Quant Electr 2010; 16(4): 730–739.
8. Luke GP, Yeager D, Emelianov SY. Biomedical applications of photoacoustic imaging with exogenous contrast agents. Ann Biomed Eng 2011; 1–16.
9. Eghtedari M, Oraevsky A, Copland JA, Kotov NA, Conjusteau A, Motamedi M. High sensitivity of in vivo detection of gold nanorods using a laser optoacoustic imaging system. Nano Lett 2007; 7(7): 1914–1918.
10. Manohar S, Ungureanu C, Van Leeuwen TG. Gold nanorods as molecular contrast agents in photoacoustic imaging: the promises and the caveats. Contrast Media Mol Imag 2011; 6(5): 389–400.
11. De la Zerda A, Kim J-W, Galanzha EI, Gambhir SS, Zharov VP. Advanced contrast nanoagents for photoacoustic molecular imaging, cytometry, blood test and photothermal theranostics. Contrast Media Mol Imag 2011; 6(5): 346–369.
12. McCormack DR, Bhattacharyya K, Kannan R, Katti K, Viator JA. Enhanced photoacoustic detection of melanoma cells using gold nanoparticles. Lasers Surg Med 2011; 43(4): 333–338.
13. Li W, Brown PK, Wang LV, Xia Y. Gold nanocages as contrast agents for photoacoustic imaging. Contrast Media Mol Imag 2011; 6(5): 370–377.
14. Song KH , Kim C, Cobley CM, Xia Y, Wang LV. Near-infrared gold nanocages as a new class of tracers for photoacoustic sentinel lymph node mapping on a rat model. Nano Lett 2009; 9(1): 183–188.
15. Yang X, Skrabalak SE, Li Z, Xia Y, Wang LV. Photoacoustic tomography of a rat cerebral cortex in vivo with au nanocages as an optical contrast agent. Nano Lett 2007; 7(12): 3798–3802.
16. De la Zerda A, Liu Z, Bodapati S, Teed R, Vaithilingam S, Khuri-Yakub BT, Chen X, Dai H, Gambhir SS. Ultrahigh sensitivity carbon nanotube agents for photoacoustic molecular imaging in living mice. Nano Lett 2010; 10(6): 2168–2172.
17. Hirsch LR, Stafford RJ, Bankson JA, Sershen SR, Rivera B, Price RE, Hazle JD, Halas NJ, West JL. Nanoshell-mediated near-infrared thermal therapy of tumors under magnetic resonance guidance. Proc Natl Acad Sci USA 2003; 100(23): 13549–13554.
18. Fu K, Sun J, Lin H, Alex W, Wang H, Halas NJ, Drezek RA. Polarized angular dependent light scattering properties of bare and pegylated gold nanoshells. Curr Nanosci 2007; 3(2): 167–170.
19. Weissleder R, Elizondo G, Josephson L, Compton CC, Fretz CJ, Stark DD, Ferrucci JT. Experimental lymph node metastases: enhanced detection with MR lymphography. Radiology 1989; 171(3): 835–839.
20. Daldrup HE, Link TM, Blasius S, Strozyk A, Könemann S, Jürgens H, Rummeny EJ. Monitoring radiation-induced changes in bone marrow histopathology with ultra-small superparamagnetic iron oxide (USPIO)-enhanced mri. J Magn Reson Imag 1999; 9(5): 643–652.
21. Metz S, Bonaterra G, Rudelius M, Settles M, Rummeny EJ, Daldrup-Link HE. Capacity of human monocytes to phagocytose approved iron oxide MR contrast agents in vitro. Eur Radiol 2004; 14(10): 1851–1858.
22. Raynal I, Prigent P, Peyramaure S, Najid A, Rebuzzi C, Corot C. Macrophage endocytosis of superparamagnetic iron oxide nanoparticles. Invest Radiol 2004; 39: 56–63.
23. Clement O, Siauve N, Cuenod CA, Frija G. Liver imaging with ferumoxides (Feridex): fundamentals, controversies, and practical aspects. Top Magn Reson Imag 1998; 9(3): 167–182.
24. Motomura K, Ishitobi M, Komoike Y, Koyama H, Noguchi A, Sumino H, Kumatani Y, Inaji H, Horinouchi T, Nakanishi K. SPIO-enhanced magnetic resonance imaging for the detection of metastases in sentinel nodes localized by computed tomography lymphography in patients with breast cancer. Ann Surg Oncol 2011; 18(12): 3422–3429.
25. Anzai Y, McLachlan S, Morris M, Saxton R, Lufkin RB. Dextran-coated superparamagnetic iron oxide, an MR contrast agent for assessing lymph nodes in the head and neck. AJNR Am J Neuroradiol 1994; 15(1): 87–94.
26. Bellin MF, Roy C, Kinkel K, Thoumas D, Zaim S, Vanel D, Tuchmann C, Richard F, Jacqmin D, Delcourt A, Challier E, Lebret T, Cluzel P. Lymph node metastases: safety and effectiveness of MR imaging with ultrasmall superparamagnetic iron oxide particles initial clinical experience. Radiology 1998; 207(3): 799–808.
27. Will O, Purkayastha S, Chan C, Athanasiou T, Darzi AW, Gedroyc W, Tekkis PP. Diagnostic precision of nanoparticle-enhanced MRI for lymph-node metastases: a meta-analysis. Lancet Oncol 2006; 7(1): 52–60
28. Schlegel A, Alvarado SF, Wachter P. Optical properties of magnetite (Fe_3O_4). J Phys C: Sol State Phys 1979; 12: 1157.
29. Mienkina MP, Friedrich C-S, Hensel K, Gerhardt NC, Hofmann MR, Schmitz G. Evaluation of ferucarbotran (Resovist) as a photoacoustic contrast agent/evaluation von ferucarbotran (Resovist) ALS photoakustisches kontrastmittel. Biomed Tech (Berl) 2009; 54(2): 83–88.
30. McLaughlin RA, Scolaro L, Robbins P, Hamza S, Saunders C, Sampson DD. Imaging of human lymph nodes using optical coherence tomography: potential for staging cancer. Cancer Res 2010; 70(7): 2579–2584.
31. Horsnell JD, Smith JA, Sattlecker M, Sammon A, Christie-Brown J, Kendall C, Stone N. Raman spectroscopy–a potential new method for the intra-operative assessment of axillary lymph nodes. Surgeon 2012; 10(3): 123–127.
32. Cengelli F, Maysinger D, Tschudi-Monnet F, Montet X, Corot C, Petri-Fink A, Hofmann H, Juillerat-Jeanneret L. Interaction of functionalized superparamagnetic iron oxide nanoparticles with brain structures. J Pharmacol Exp Ther 2006; 318(1): 108–116.
33. Wang YX, Hussain SM, Krestin GP. Superparamagnetic iron oxide contrast agents: physicochemical characteristics and applications in MR imaging. Eur Radiol 2001; 11(11): 2319–2331.

34. Aucouturier J, Dupuis L, Deville S, Ascarateil S, Ganne V. Montanide ISA 720 and 51: a new generation of water in oil emulsions as adjuvants for human vaccines. Expert Rev Vaccines 2002; 1(1): 111–118.
35. Klerkx WM, Geldof AA, Heintz AP, van Diest PJ, Visser F, Mali WP, Veldhuis WB. Longitudinal 3.0 T MRI analysis of changes in lymph node volume and apparent diffusion coefficient in an experimental animal model of metastatic and hyperplastic lymph nodes. J Magn Reson Imag 2011; 33(5): 1151–1159.
36. Jose J, Willemink RGH, Resink S, Piras D, van Hespen JC, Slump CH, Steenbergen W, van Leeuwen TG, Manohar S. Passive element enriched photoacoustic computed tomography (per pact) for simultaneous imaging of acoustic propagation properties and light absorption. Opt Express 2011; 19(3): 2093–2104.
37. Huffman DR, Bohren CF. Absorption and Scattering of Light by Small Particles. Wiley: New York, 1983.
38. Butler MF, Cameron RE. A study of the molecular relaxations in solid starch using dielectric spectroscopy. Polymer 2000; 41(6): 2249–2263.
39. Lee AS, Weissleder R, Brady TJ, Wittenberg J. Lymph nodes: microstructural anatomy at MR imaging. Radiology 1991; 178(2): 519–522.
40. Lind K, Kresse M, Debus NP, Müller RH. A novel formulation for superparamagnetic iron oxide (SPIO) particles enhancing mr lymphography: comparison of physicochemical properties and the in vivo behaviour. J Drug Target 2002; 10(3): 221–230.
41. Catalano MF, Sivak MV, Rice T, Gragg LA, Van Dam J. Endosonographic features predictive of lymph node metastasis. Gastrointest Endosc 1994; 40(4): 442–446.
42. Razansky D, Baeten J, Ntziachristos V. Sensitivity of molecular target detection by multispectral optoacoustic tomography (MSOT). Med Phys 2009; 36(3): 939–945.
43. Shao P, Cox B, Zemp RJ. Estimating optical absorption, scattering, and grueneisen distributions with multiple-illumination photoacoustic tomography. Appl Opt 2011; 50(19): 3145–3154.
44. Taupitz M, Wagner S, Hamm B, Binder A, Pfefferer D. Interstitial mr lymphography with iron oxide particles: results in tumor-free and VX2 tumor-bearing rabbits. AJR Am J Roentgenol 1993; 161(1): 193–200.
45. Heesakkers RAM, Hovels AM, Jager GJ, van den Bosch HCM, Witjes JA, Raat HPJ, Severens JL, Adang EMM, van der Kaa CH, Futterer JJ, Barentsz J. MRI with a lymph-node-specific contrast agent as an alternative to CT scan and lymph-node dissection in patients with prostate cancer: a prospective multicohort study. Lancet Oncol 2008; 9(9): 850–856.
46. Harisinghani MG, Barentsz J, Hahn PF, Deserno WM, Tabatabaei S, van de Kaa CH, de la Rosette J, Weissleder R. Noninvasive detection of clinically occult lymph-node metastases in prostate cancer. New Engl J Med 2003; 348(25): 2491–2499.
47. Haraszczuk R, Nurzynska K. Photoacoustic detection of sentinel lymph node with sensor array. J Med Inform Technol 2011; 17: 1642–6037.
48. Qu M, Mallidi S, Mehrmohammadi M, Truby R, Homan K, Joshi P, Chen YS, Sokolov K, Emelianov S. Magneto-photo-acoustic imaging. Biomed Opt Express 2011; 2(2): 385–395.
49. Qu M, Mehrmohammadi M, Emelianov S. Detection of nanoparticle endocytosis using magneto-photoacoustic imaging. Small 2011; 7: 2858–2862.
50. Kim C, Erpelding TN, Jankovic L, Pashley MD, Wang LV. Deeply penetrating in vivo photoacoustic imaging using a clinical ultrasound array system. Biomed Opt Express 2010; 1(1): 278–284.
51. Kim C, Erpelding TN, Jankovic L, Wang LV. Performance benchmarks of an array-based hand-held photoacoustic probe adapted from a clinical ultrasound system for non-invasive sentinel lymph node imaging. Phil Trans A Math Phys Eng Sci 2011; 369(1955): 4644–4650.